This is a repository copy of *Modelling extreme ultraviolet ablation interactions*.

White Rose Research Online URL for this paper:
https://eprints.whiterose.ac.uk/149056/

Version: Published Version

Proceedings Paper:
Lolley, James, Wilson, Sarah Arabella orcid.org/0000-0001-5914-5085 and Tallents, Gregory John orcid.org/0000-0002-1409-105X (2019) Modelling extreme ultraviolet ablation interactions. In: Proceedings Volume 11035, Optics Damage and Materials Processing by EUV/X-ray Radiation VII; 110350R (2019). SPIE , R1- R8.

https://doi.org/10.1117/12.2523137

Reuse
Items deposited in White Rose Research Online are protected by copyright, with all rights reserved unless indicated otherwise. They may be downloaded and/or printed for private study, or other acts as permitted by national copyright laws. The publisher or other rights holders may allow further reproduction and re-use of the full text version. This is indicated by the licence information on the White Rose Research Online record for the item.

Takedown
If you consider content in White Rose Research Online to be in breach of UK law, please notify us by emailing eprints@whiterose.ac.uk including the URL of the record and the reason for the withdrawal request.

eprints@whiterose.ac.uk
https://eprints.whiterose.ac.uk/

PROCEEDINGS OF SPIE

SPIEDigitalLibrary.org/conference-proceedings-of-spie

Modelling extreme ultraviolet ablation interactions

J. A. Lolley, S. A. Wilson, G. J. Tallents

J. A. Lolley, S. A. Wilson, G. J. Tallents, "Modelling extreme ultraviolet ablation interactions," Proc. SPIE 11035, Optics Damage and Materials Processing by EUV/X-ray Radiation VII, 110350R (24 April 2019); doi: 10.1117/12.2523137

SPIE.

Event: SPIE Optics + Optoelectronics, 2019, Prague, Czech Republic

Downloaded From: https://www.spiedigitallibrary.org/conference-proceedings-of-spie on 20 May 2019 Terms of Use: https://www.spiedigitallibrary.org/terms-of-use

Invited Paper

Modeling extreme ultraviolet ablation interactions

J A Lolley, S A Wilson, G J Tallents

York Plasma Institute, Department of Physics, University of York, York, UK

ABSTRACT

Compact extreme ultraviolet (EUV) laser sources can be used for laboratory-scale ablation experiments at intensities of $1 \times 10^{11}\,\mathrm{W\,cm^{-2}}$ and higher. The depths of ablation achieved using focused laser output at 46.9 nm to irradiate solid targets of aluminium, gold, and copper have been modeled. Two simple models are considered; an adaptation of an ultra-short pulse model, and an ablation velocity model. We show that the attenuation length of the material plays an important role in the physics of the ablation. A more detailed one-dimensional model including absorption by inverse bremsstrahlung absorption and photo-ionization, corrected to include electron degeneracy effects, is used to evaluate the opacity of the ablation plasma and subsequent ablation depths.

Keywords: ablation, short-wavelength, EUV, theory

1. INTRODUCTION

The field of short wavelength lasing expanded rapidly after the first source was developed at the Lawrence Livermore National Laboratory (LLNL) in the mid 1980s[1]. Subsequent developments in table-top and compact sources of high pulse energies[2;3] have resulted in increased interest in the interaction between short wavelength radiation and solid materials. Short wavelength radiation interactions with solid targets are important in indirect drive inertial confinement fusion (ICF), where extreme ultra-violet (EUV) and x-ray radiation in a hohlraum drives the implosion of a pellet containing deuterium-tritium fuel. EUV interactions differ from harder x-ray interactions because of the typically higher absorption into solid material at the reduced photon energy.

EUV radiation is used in a variety of materials processing applications, the most significant of which is EUV lithography[4]. This process uses photo-resist material and EUV radiation to etch features via a mask onto silicon wafers. This technology uses incoherent EUV laser-plasma sources emitting at 13.5 nm as strong emissions at this wavelength occur in both lithium and tin, and silicon/molybdenum mirrors have a peak reflectivity here. For some applications, a coherent source with considerably lower divergence could be beneficial in directly ablating solids.

The motivation for this work is to understand more clearly the ablation mechanisms occurring in experiments conducted using an EUV capillary discharge laser[2;3] emitting radiation at 46.9 nm. An experiment is modeled where EUV radiation is focused onto a solid target using an in-line multi-layer spherical mirror with a reflectivity of approximately 40%. The investigation assumes laser pulse energies up to $\approx 20\,\mu\mathrm{J}$ on target and focal spot diameters in the 1 µm to 6 µm range.

2. CHARACTERISTICS OF EUV ABLATION

2.1. EUV absorption mechanisms

Compared to optical laser interactions, laser-solid interactions in the EUV regime result in different absorption behavior due to the increase in photon energy. The critical density increases, and single photon photo-ionization becomes an important absorption process. The plasma critical density, n_{crit}, is the electron density at which the

Optics Damage and Materials Processing by EUV/X-ray Radiation VII, edited by Libor Juha, Saša Bajt, Stéphane Guizard,
Proc. of SPIE Vol. 11035, 110350R · © 2019 SPIE · CCC code: 0277-786X/19/$18 · doi: 10.1117/12.2523137

Downloaded From: https://www.spiedigitallibrary.org/conference-proceedings-of-spie on 20 May 2019
Terms of Use: https://www.spiedigitallibrary.org/terms-of-use

plasma frequency and laser frequency are equal and is given by

$$n_{crit} = \frac{\epsilon_0 m_e \omega_L^2}{e^2} \tag{1}$$

where ω_L is the laser frequency. In optical laser interactions, the critical density marks the limit of laser penetration into the target and the typical density for which laser energy is absorbed by resonant absorption and other collective absorption effects. At short wavelengths, the critical density is above the density of the solid target; as a result this penetration limit no longer applies and resonance absorption does not occur.

The absorption coefficient for inverse bremsstrahlung, or free-free, absorption can be found by calculating black body emission due to bremsstrahlung and then using detailed balance to find the absorption coefficient. This is a treatment used by Hutchinson[5] and Tallents[6]. The free-free absorption coefficient, K_{ff}, can then be found as

$$K_{ff} = 8\sqrt{\pi}\left(\frac{e^2}{4\pi\epsilon_0}\right)^3 \frac{4}{3c^3}\left(\frac{Z}{m_e}\right)^2 n_e n_{Z+1}\left(\frac{m_e}{2k_B T}\right)^{1/2} \frac{\pi^2 c^2}{\hbar\omega^3}\left(1-\exp\left(-\frac{\hbar\omega}{k_B T}\right)\right)\frac{1}{\sqrt{3}} \tag{2}$$

where Z and T are the plasma ionization and temperature, ω is the frequency of the incident radiation, and all other constants have their usual meanings. The factor $1/\sqrt{3}$ is a correction known as the Kramers correction[7] that results from the hyperbolic geometry of the interaction. The same treatment can also be applied to photo-ionization, or bound-free absorption[5;6]. This gives the bound-free absorption coefficient as

$$K_{bf} = \sigma_{bf} n_Z = \frac{16}{3\pi}\frac{g_{Z+1}}{g_Z}\alpha^3 \frac{\pi^2 c^2}{\hbar\omega}\left[\frac{2R_y Z^4}{n^3}\right]\frac{1}{\sqrt{3}} n_Z \tag{3}$$

where α is the fine structure constant $\approx 1/137$, R_y is the Rydberg energy in eV, n is the principal quantum number of the ionization state. The ratio of degeneracies g_{Z+1}/g_Z can be approximated to $1/n^2$ which then yields an overall $1/n^5$ dependence for K_{bf}.

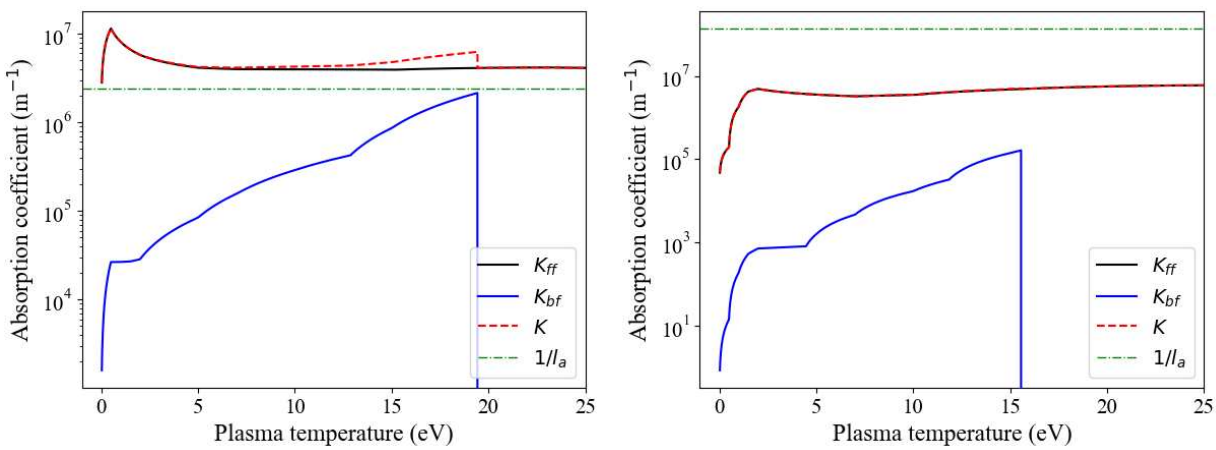

(a) Aluminium (b) Gold

Figure 1: K_{ff} and K_{bf} absorption coefficients for aluminium and gold (neglecting electron degeneracy effects) as a function of plasma temperature. K is the sum of K_{bf} and K_{ff}. $1/l_a$ is the reciprocal of the solid material attenuation length and is used as the solid absorption coefficient.

Comparison of the coefficients K_{ff} and K_{bf} requires knowledge of both the plasma temperature and average ionization. This is modeled by the collisional-radiative code FLYCHK[8], assuming a constant plasma density equal to solid density. Both absorption coefficients are plotted, for the cases of gold and aluminium, in figure 1. Also shown is the effective absorption coefficient of the solid material, calculated from tabulated values[9] by taking the reciprocal of the attenuation length l_a, for comparison between the two states (solid and plasma). As figure 1 shows, the contribution of photo-ionization to the overall absorption mechanism is material dependent and only of significance in aluminium. The horizontal line represents the reciprocal of the solid attenuation length.

Downloaded From: https://www.spiedigitallibrary.org/conference-proceedings-of-spie on 20 May 2019
Terms of Use: https://www.spiedigitallibrary.org/terms-of-use

2.2. High density effects

At solid densities, plasma created by EUV laser light has free electrons affected by degeneracy. The free quantum states are close to full, so the Fermi-Dirac distribution, rather than a Maxwellian distribution, occurs. Considering free-free absorption, a degeneracy correction factor can be calculated, given by

$$\frac{K^*_{ff}}{K_{ff}} = \frac{\int_{\hbar\omega}^{\infty} \frac{1}{E^{1/2}} f_{FD}(E) P(E-\hbar\omega) dE}{\int_{\hbar\omega}^{\infty} \frac{1}{E^{1/2}} f_M(E) dE} \tag{4}$$

where f_{FD} is the Fermi-Dirac distribution, f_M is the Maxwell-Boltzmann distribution, and $P(E-\hbar\omega)$ is known as the 'blocking factor', which expresses the probability of specific quantum states being filled. The blocking factor is given by

$$P(E-\hbar\omega) = 1 - \frac{1}{\exp(-\eta + x - \beta) + 1} \tag{5}$$

where η is the reduced chemical potential μ/k_BT, x is the reduced energy E/k_BT, and β is the reduced photon energy $\hbar\omega/k_BT$. The degeneracy correection factor can be evaluated as

$$\frac{K^*_{ff}}{K_{ff}} = \frac{1}{\exp(\eta-\beta)} \int_{\beta}^{\infty} \frac{1}{1+\exp(-\eta+x)} \left[1 - \frac{1}{1+\exp(-\eta+x-\beta)}\right] dx. \tag{6}$$

Using a similar logic, the bound-free absorption coefficient can be adjusted by considering degeneracy effects. In this case, it is simply a matter of adjusting the photo-ionization cross-section, again using the blocking factor $P(E-\hbar\omega)$, this time with respect to the reduced ionization energy, x_{ion};

$$\frac{\sigma^*_{bf}}{\sigma_{bf}} = \frac{K^*_{bf}}{K_{bf}} = P(E-\hbar\omega) = 1 - \frac{1}{\exp(-\eta + x_{ion} - \beta)}. \tag{7}$$

The above corrections can then be combined with our existing expressions for the free-free and bound-free absorption coefficients to give a degeneracy-corrected absorption coefficient, as shown in figure 2.

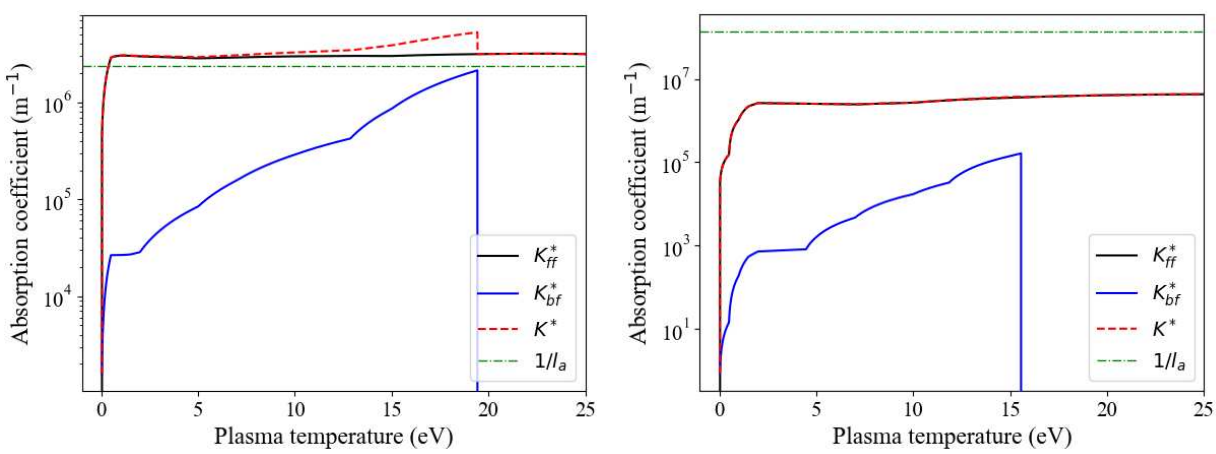

(a) Aluminium (b) Gold

Figure 2: K^*_{ff} and K^*_{bf} absorption coefficients for aluminium and gold (including electron degeneracy effects) as a function of plasma temperature, adjusted to include degeneracy . K^* is the sum of K^*_{bf} and K^*_{ff}. $1/l_a$ is the reciprocal of the solid material attenuation length and is used as the solid absorption coefficient.

As in figure 1, there are material-specific differences in the absorption coefficients, and the changes brought about by the degeneracy corrections are most pronounced in aluminium. Given that resonant absorption and other collective absorption mechanisms are no longer part of the absorption model, it is likely that the plasma

Downloaded From: https://www.spiedigitallibrary.org/conference-proceedings-of-spie on 20 May 2019
Terms of Use: https://www.spiedigitallibrary.org/terms-of-use

temperatures achieved will be considerably lower than those found in visible/infra-red wavelength ablation. Ablation plasma temperatures are, therefore, in the region of figure 2 where both degeneracy and the contribution of photo-ionization are significant, particularly in the case of aluminium.

Codes used to simulate laser-plasma interactions primarily rely solely on inverse bremsstrahlung absorption and neglect degeneracy. This is a valid model for visible/infra-red wavelength interactions because these processes are not active due to the lower photon energy and plasma density. EUV ablation requires the development of new models that include these processes.

3. SIMPLE MODELS

From the absorption investigation above, it is clear that the ablation behavior of the two metals we are considering, gold and aluminium, will differ significantly and will likely require different absorption models. We will first consider the short attenuation length case of gold.

3.1. Short attenuation lengths

As can be seen from figure 2, the effective absorption coefficient of solid gold, calculated as $1/l_a$, is greater by at least an order of magnitude than the calculated absorption coefficient for plasma at solid density. This means that the photon absorption once the plasma has been created is small, and at low plasma temperatures negligible, by comparison to the solid. By making an assumption that absorption can be neglected once the plasma is generated, or once the deposited energy exceeds a certain value, an existing ablation model can be recovered as an approximate expression.

The model in question is the bleaching wave model[10], which proposes that energy is deposited into the solid in a thin layer, making it transparent ('bleached'). The radiation then deposits energy into the next thin layer, and so on, generating a 'bleaching wave' that propagates into the target with some velocity v. The energy deposited into this layer is given by

$$H_{bl}dx = Idt \tag{8}$$

where H_{bl} is the bleaching energy density, and from this the ablation depth can be extracted to give

$$d_{abl} = \int dx = \int \frac{Idt}{H_{bl}} = \frac{F}{H_{bl}}. \tag{9}$$

This bleaching energy density is given by

$$H_{bl} = H_{abl} + \frac{\rho}{Am_p}\left[\frac{3}{2}(Z_i+1)k_BT + \sum_{Z'=1}^{Z}(E_{ion}(Z'))\right] \tag{10}$$

where H_{abl} is the latent heat of ablation (fusion + vaporization), and $E_{ion}(Z')$ is the ionization energy of a given ionization state Z'. Z is defined from the average ionization Z_i, calculated by FLYCHK for a plasma of temperature T at solid density. In order to more accurately assess the energy content, fractional abundances are calculated for the ionization states above and below Z_i. Two values for Z are then defined and are summed, such that $Z_1f_1 + Z_2f_2 = Z_i$ where f_1 and f_2 are the fractional abundances of the higher and lower ionization states.

This model makes assumptions other than neglecting the absorption of the generated plasma. It includes no ablation threshold, an assumption that would not be valid for longer wavelength ablation. The inclusion of photo-ionization means that some amount of ablation can occur with just a very small number of photons. It is plausible this means there is no lower fluence ablation limit.

3.2. Long attenuation lengths

From figure 2a for aluminium, it is clear that the model described above is not going to be an accurate approximation, given that the plasma absorption coefficient exceeds the effective absorption coefficient of the solid in a relevant temperature range. A simple alternative is proposed that is based on the Gamaly ultra-short (fs) pulse

Downloaded From: https://www.spiedigitallibrary.org/conference-proceedings-of-spie on 20 May 2019
Terms of Use: https://www.spiedigitallibrary.org/terms-of-use

model[11]. By replacing the 'skin depth' l_s with the attenuation length l_a, an expression for the change in fluence with penetration depth can be found

$$F = F_{abl} \exp\left(-\frac{x}{l_a}\right) \tag{11}$$

where F_{abl} is the threshold fluence for ablation. This can then be rearranged to predict the ablation depth d, given by

$$d = l_a \ln\left(\frac{F}{F_{abl}}\right). \tag{12}$$

As mentioned above, this model was originally developed for short pulse interactions. The assumption made is that the effects of hydrodynamic expansion are negligible and the generation of plasma has a negligible effect on the absorption coefficient. The latter assumption only works in this long attenuation length case where $1/l_a$ is of the same order as the plasma absorption, as in figure 2a. By consulting figure 2a, we can predict an under-prediction in ablation depths from this model as the plasma absorption coefficient exceeds the solid equivalent throughout the majority of the temperature range.

4. DEVELOPMENT OF EUVED ALGORITHM

The simple models detailed above are limited as they ignore the absorption of the EUV laser light once a plasma forms. Here we describe a model that includes this absorption, named EUVED (Extreme Ultra-Violet Energy Deposition). Using equations 2, 3, 6, and 7, a plasma absorption coefficient can be calculated and used to determine the transparency of a given volume at temperatures corresponding to energy densities above the bleaching energy density.

The EUVED algorithm starts by initializing a series of cylindrical spatial cells with dimensions dx x A_{spot} (where dx is the cell length and A_{spot} is the focal spot area) at room temperature and solid density. To calculate the energy deposition, the absorption coefficient is used to evaluate the change in intensity across each spatial cell dI_n (regardless of cell state) according to

$$dI_n = I_{n-1}[1 - \exp(-K_n dx)] \tag{13}$$

where I_{n-1} is the intensity arriving at the left-most edge of the cell (i.e. the intensity leaving the previous cell) and K_n is the total absorption coefficient for the cell. Assuming a $\sin^2(x)$ pulse shape, integrating the intensity from t to $t + dt$ yields the energy deposited into the cell per time-step, dE_n, as

$$dE_n = \frac{1}{4\pi}\left(t_{pulse}\left[\sin\left(\frac{2\pi t}{t_{pulse}}\right) - \sin\left(\frac{2\pi(t+dt)}{t_{pulse}}\right)\right] + 2\pi dt\right) dI_n A_{spot} \tag{14}$$

where t_{pulse} is the laser pulse time. This process then repeats, with the new cell energy E_n being used to update the cell temperature, T_n, and absorption coefficient, K_n, so that the energy deposition in the next time-step can be calculated. The code dumps key values (position x, temperature T_n, ionization $Z_{i,n}$, absorption coefficient K_n, and energy E_n) for each cell to file at regular intervals and at the end of the algorithm the deposited energy is checked against E_{pulse} for consistency.

The algorithm progresses in time by first checking the state of each cell; solid or plasma. This is determined by comparing the cell energy E_n to a 'switching energy' E_s, above which the plasma model of absorption is used. In the solid state, the solid absorption coefficient ($1/l_a$) is used to calculate energy deposition. In the plasma state, the cell energy E_n is first used to update the temperature T_n of the cell, from which the values for ionization $Z_{i,n}$ and absorption coefficient K_n are then calculated using equations 2, 3, 6, and 7. The photo-ionization absorption coefficient is only evaluated up to ionizations with ionization energy less than the photon energy, above which photo-ionization switches off. Temperatures are determined by comparing E_n with the energy content, calculated using equation 10.

This model effectively takes the bleaching wave model and resolves the temporal evolution of the wave instead of assuming linear progress. There are still limitations – the lack of material flow means that energy deposition may be overestimated, as both K_{ff} and K_{bf} have density dependencies. There would also be an inherent cooling that occurs as the plasma expands, further changing the absorption coefficients. The significance of the impact

Downloaded From: https://www.spiedigitallibrary.org/conference-proceedings-of-spie on 20 May 2019
Terms of Use: https://www.spiedigitallibrary.org/terms-of-use

of flow can be evaluated by calculating the sound speed of the plasma and using this to determine the distance the plasma ions are likely to cover in the pulse time. The sound speed v_s is given by

$$v_s = \sqrt{\frac{\gamma Z_i k_B T}{M m_p}} \tag{15}$$

where γ is the adiabatic index $\frac{5}{3}$ and M is the mass number of the ion. Taking a temperature of 10 eV, the sound speed v_s is found to have values in the range $1 \times 10^3\,\mathrm{m\,s^{-1}}$ to $1 \times 10^4\,\mathrm{m\,s^{-1}}$, corresponding to a distance of 1 µm to 10 µm during the pulse duration (depending on the mass of the ions). This result is of approximately the same order as the ablation depth, so this flow may be considered significant. A detailed comparison with a suitable hydrodynamic code would resolve this, provided that code could be adjusted to incorporate the same absorption physics.

Another limitation of the code is the lack of definition for the switching energy E_s. In its current state, this is best treated as a fitting parameter that is adjusted to fit experimental ablation depths. Possible suggestions for E_s include the energy content for a plasma at the vaporization temperature of the material, or the energy content for when the plasma is fully singly ionized ($Z_i \geq 1$). This value would be further changed if the common assumption of initial ionization was to be implemented (3+ for aluminium and 1+ for gold).

5. RESULTS AND MODEL COMPARISON

The effect of changing the switching energy on the ablated depth has been investigated. The ablation depth is defined as the cumulative length of the cells that have been converted to plasma by the end of the algorithm. Figure 3 shows the simulated ablation depths for aluminium and gold, with copper also shown to act as an

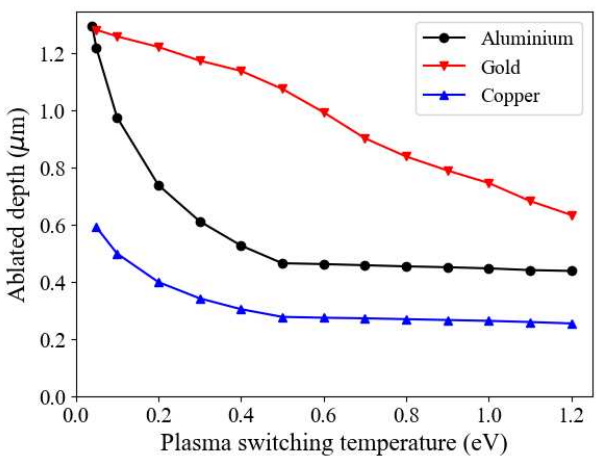

Figure 3: Simulated ablation depth as a function of switching temperature (switching energy is calculated as energy content at this temperature). Pulse energy is 20 µJ and focal spot size is 5.65 µm.

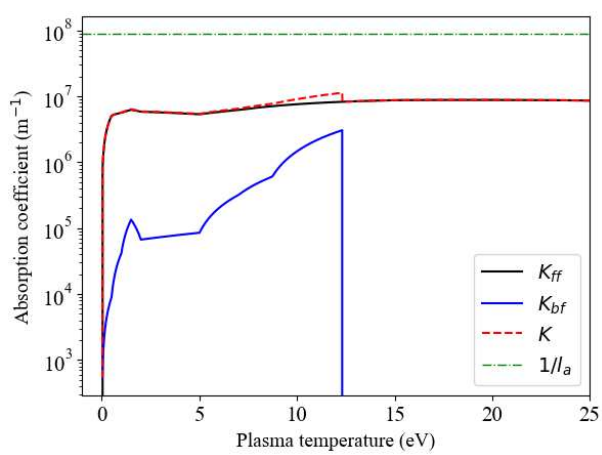

Figure 4: K^*_{ff}, K^*_{bf}, and K^* (including electron degeneracy effects) for copper as a function of plasma temperature. $1/l_a$ is show for comparison.

intermediate (the materials have $l_a = 419$ nm, 7.2 nm, and 11.2 nm respectively), as a function of the temperature T_s corresponding to a specific E_s. For reference, the absorption coefficients for copper are shown in figure 4. The pulse energy was fixed at 20 µJ with a spot diameter of 5.65 µm. As was expected, the ablated depth decreases as T_s increases, however the shape of this dependence is interesting. Energy deposition is of the form e^{-x} (with x the distance into the target), so increasing E_s should decrease the ablated depth with a similar form. This is broadly the case for aluminium. For gold however, the dependence on E_S is much closer to linear. If the EUVED model can be approximated to the bleaching wave model, the switching energy E_s can be equated to

Downloaded From: https://www.spiedigitallibrary.org/conference-proceedings-of-spie on 20 May 2019
Terms of Use: https://www.spiedigitallibrary.org/terms-of-use

the bleaching energy E_{bl} ($H_{bl} \times V_{cell}$), and the roughly linear decrease in ablation depth with E_s is recovered. The ablation depth behavior of the copper targets is interesting as it follows that of the aluminium more closely, despite having absorption coefficients much more similar to gold (i.e. an order of magnitude difference between the solid and plasma states).

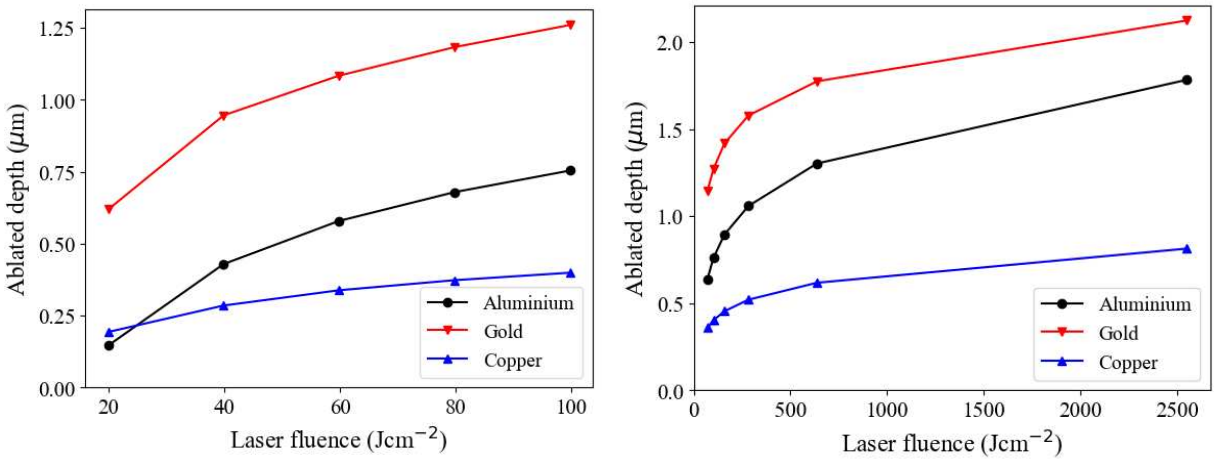

(a) Pulse energies from 5 µJ to 25 µJ.

(b) Spot diameters from 1 µm to 6 µm.

Figure 5: Ablation depths as a function of laser fluence across different ranges. The switching energy was set at the energy for vaporization for a cell volume.

The fluence dependence of the ablation depth, particularly with reference to the simple models mentioned in section 3, is shown in figure 5 and was evaluated by adjusting two parameters; pulse energy E_{pulse} (figure 5a) and focal spot size A_{spot} (figure 5b). For the purpose of this investigation, the switching energy was fixed at the material dependent vaporization energy for one cell volume. As figure 5b shows, a linear change in focal spot diameter, causing an r^2 change in A_{spot}, causes an approximately $d^{-1/2}$ change in the ablated depth. This is as would be expected, with deviation from this accounted for in the variation from linear behavior seen in figure 5a. These tests not only produce predictions over two very different fluence ranges, they also show that the internal fluence and intensity calculations performed by the code are functioning as expected.

The dependencies shown in figures 3 and 5 broadly support the assertions made by the simple models in section 3, however the predicted fluence dependencies in figure 5 do suggest a more complex picture. The switching dependency of ablated depth for the aluminium suggests that energy is deposited approximately exponentially, as is predicted by the Gamaly model adaptation. The subsequent fluence dependency deviates from this however, appearing somewhere between a linear and logarithmic trend. For the gold, again, the switching dependence of ablated depth is roughly linear, as would be expected, but the fluence dependence of the ablated depth deviates from this with a trend somewhere between linear and logarithmic. Comparison with experimental data will help to determine the accuracy of these predictions.

6. CONCLUSIONS

Some simple one-dimensional ablation depth models have been constructed by examining the plasma absorption coefficients for a variety of metals – namely gold, copper and aluminium. In the case where the solid material has a short attenuation length, a bleaching wave model is suggested. An examination of the energy deposition using the hydro-static EUVED code has shown this to be a valid approximation, as plasma absorption coefficients are much smaller than tabulated solid, room temperature absorption coefficients. When the attenuation length is long, a model based on the Gamaly ultra-short optical pulse ablation values is suggested. The EUVED code, where the absorption of plasma material material is considered in ablation depth modeling is being bench-marked against experimental results. Experimental ablation depths will be used to determine appropriate switching energies,

Downloaded From: https://www.spiedigitallibrary.org/conference-proceedings-of-spie on 20 May 2019
Terms of Use: https://www.spiedigitallibrary.org/terms-of-use

where the absorption coefficient for the laser radiation changes from tabulated solid values to those calculated for a solid density plasma.

References

[1] Matthews, D. L. et al., "Demonstration of a Soft X-ray Amplifier," *Physical Review Letters* **54**, 110 (1985).

[2] Benware, B. R., Macchietto, C. D., Moreno, C. H., and Rocca, J. J., "Demonstration of a High Average Power Tabletop Soft X-Ray Laser," *Physical Review Letters* **81**(26), 5804 (1998).

[3] Rocca, J. J. et al., "Discharge-pumped soft x-ray laser in neon-like argon," *Physics of Plasmas* **2**, 2547 (1995).

[4] Tallents, G., Wagenaars, E., and Pert, G., "Lithography at EUV wavelengths," *Nature Photonics* **4**, 809 (2010).

[5] Hutchinson, I., [*Principles of Plasma Diagnostics*] (2005).

[6] Tallents, G. J., [*An Introduction to the Atomic and Radiation Physics of Plasmas*] (2018).

[7] Kramers, H. A., "On the theory of X-ray absorption and of the continuous X-ray spectrum," *Philosophical Magazine* **46**, 836 (1923).

[8] Chung, H. K. et al., "FLYCHK: Generalized population kinetics and spectral model for rapid spectroscopic analysis for all elements," *High Energy Density Physics* **1**(1), 3 (2005).

[9] Henke, B. L., Gulikson, E. M., and Davis, J. C., "X-ray interactions: photoabsorption, scattering, transmission, and reflection at E=50-30000 eV, Z=1-92," *Atomic Data and Nuclear Data Tables* **54**(2), 181 (1993).

[10] Tallents, G. J., Whittaker, D. S., Wilson, L. A., and Wagenaars, E., "Heating of high energy density plasmas using EUV and x-ray lasers," in [*Proceedings of SPIE: X-ray Lasers and Coherent X-ray Sources: Development and Applications IX*], **8140** (2011).

[11] Gamaly, E. G., Rode, A. V., and Luther-Davies, B., "Ablation of solids by femtosecond lasers: Ablation mechanism and ablation thresholds for metals and dielectrics," *Physics of Plasmas* **9**, 949 (2002).

Downloaded From: https://www.spiedigitallibrary.org/conference-proceedings-of-spie on 20 May 2019
Terms of Use: https://www.spiedigitallibrary.org/terms-of-use